

The growth history of local M33-mass bulgeless spiral galaxies

Xiaoyu Kang^{1,2,3}, Rolf-Peter Kudritzki^{4,5}, and Fenghui Zhang^{1,2,3}

¹ Yunnan Observatories, Chinese Academy of Sciences, 396 Yangfangwang, Guandu District, Kunming, 650216, P.R. China
e-mail: kxyysl@ynao.ac.cn

² Key Laboratory for the Structure and Evolution of Celestial Objects, Chinese Academy of Sciences, 396 Yangfangwang, Guandu District, Kunming, 650216, P. R. China

³ International Centre of Supernovae, Yunnan Key Laboratory, Kunming 650216, P. R. China

⁴ LMU München, Universitätssternwarte, Scheinerstr. 1, 81679 München, Germany

⁵ Institute for Astronomy, University of Hawaii, 2680 Woodlawn Drive, Honolulu, HI96822, USA

Received August 9, 2023; accepted September 14, 2023

ABSTRACT

NGC 7793, NGC 300, M33 and NGC 2403 are four nearby undisturbed and bulgeless low-mass spiral galaxies with similar morphology and stellar mass. They are ideal laboratories to study disc formation scenarios and stellar mass growth histories. We construct a simple chemical evolution model by assuming that discs grow gradually with continuous metal-free gas infall and metal-enriched gas outflow. By means of the classical χ^2 methodology, applied to the model predictions, the best combination of free parameters capable of reproducing the corresponding present-day observations is determined, i.e. the radial dependence of the infall timescale $\tau = 0.1r/R_d + 3.4$ Gyr (R_d is the disc scale-length) and the gas outflow efficiency $b_{\text{out}} = 0.2$. The model results are in excellent agreement with the general predictions of the inside-out growth scenario for the evolution of spiral galaxies. About 80% of the stellar mass of NGC 7793 is assembled within the last 8 Gyr and 40% within the last 4 Gyr. By comparing the best-fitting model results of the three other galaxies we obtain similar results, 72% (NGC 300), 66% (NGC 2403) and 79% (M33) stellar mass were assembled within the past ~ 8 Gyr (i.e. $z = 1$). These four disc galaxies simultaneously increase their sizes and stellar masses as time goes by and they grow in size at ~ 0.30 times the rate at which they grow in mass. The scale-lengths of these four discs are now 20% – 25% larger than at $z = 1$. Our best-fitting model predicted the stellar mass-metallicity relation and the metallicity gradients, constrained by the observed metallicities from HII-regions emission line analysis, agree well with the observations measured from individual massive red and blue supergiant stars and population synthesis of SDSS galaxies.

Key words. galaxies: evolution – galaxies: individual: NGC 7793 – galaxies: individual: NGC 2403 – galaxies: individual: NGC 300 – galaxies: individual: M33 – galaxies: spiral

1. Introduction

Understanding how galaxies assemble is crucial to understanding the overall picture of galaxy evolution. Spiral galaxies have a major role in the universe today, with disc galaxies dominating star formation in the present epoch (Brinchmann et al. 2004; Williams et al. 2011) and keeping forming stars at a sustained rate throughout their evolution (Aumer & Binney 2009; Fraternali & Tomassetti 2012; Pezzulli et al. 2015). At the same time, the structure and star formation history (SFH) of disc galaxies are tightly linked with stellar mass (Casasola et al. 2017), and galaxies with stellar masses near or below Milky Way-mass ($\log(M_{\text{MW},*}/M_{\odot}) \sim 10.7$) assemble their mass mainly from in situ star formation, not from mergers (Leitner & Kravtsov 2011; Qu et al. 2017; Behroozi et al. 2019; Pan et al. 2019). Furthermore, recent studies about deep surveys detecting galaxy masses ($\log(M_{*}/M_{\odot}) < 10$) have shown that very large populations low-mass galaxies exist at all redshifts and galaxy stellar mass functions exhibit a slightly steeper low-mass end (Baldry et al. 2008, 2012; Bauer et al. 2013; Kelvin et al. 2014), emphasizing a necessity to understand the growth of low-mass galaxies, the most populous in the universe.

Most of spiral galaxies are difficult to study in detail due to the complexities of their bulges (Byun & Freeman 1995) or mergers (Barnes & Hernquist 1992). While bulge-

less discs appear to be excellent laboratories to study the secular evolution of galactic discs, most of them are too distant to study in great detail. Fortunately, in the nearby Universe ($D < 4$ Mpc), there are four undisturbed and bulgeless (pure-disc) galaxies with similar morphology and stellar mass ($\log(M_{*}/M_{\odot}) < 10$): NGC 7793 (Sacchi et al. 2019), NGC 300 (Gogarten et al. 2010), M33 (Williams et al. 2009) and NGC 2403 (Williams et al. 2013). The wealth of available data including both local and global data, such as gas mass, star formation rate (SFR), stellar mass (e.g. Leroy et al. 2008), gas-phase metallicity (e.g. Pilyugin et al. 2014) and specific SFR (sSFR, Muñoz-Mateos et al. 2007; Smith et al. 2021), for these four low-mass spiral galaxies can be used to constrain their theoretical models, therefore we can use their theoretical results to compare the detailed evolution of these discs. Such comparative studies offer an ideal opportunity to search for clues to the processes that drive the galaxy disc growth histories, for instance, inside-out formation scenario, namely that the inner parts of the galaxy disc forms faster than the outer ones (e.g. Larson 1976; Matteucci & Francois 1989; Chiappini et al. 2001; Grisoni et al. 2018; Frankel et al. 2019; Spitoni et al. 2021a).

On the other hand, observations in local star-forming galaxies have revealed the existence of a tight relation between stellar mass and gas metallicity: the stellar mass-metallicity relation (MZR), with the more massive galaxies being more metal

enriched (e.g. Tremonti et al. 2004; Kewley & Ellison 2008; Andrews & Martini 2013; Zahid et al. 2014, among many others). As for the stellar metallicity, the MZR is also found in star-forming galaxies (e.g. Gallazzi et al. 2005; Panter et al. 2008; Thomas et al. 2010; Zahid et al. 2017; Sextl et al. 2023). Bresolin et al. (2022) updated the MZR based on metallicity studies of stars in resolved star-forming galaxies. The MZR seems to be a Rosetta stone for understanding the formation and evolution of galaxies.

In addition to the global metallicities, the radial gradient in metallicity is also important to understand the formation history of galaxies. After the pioneering work by Aller (1942), the radial metallicity gradient has been studied for a long time. Based on long-slit spectroscopy and Integral field unit (IFU) spectroscopy, most spiral galaxies in the local Universe exhibit negative metallicity gradients in gas and stars within their optical radius, that is, the centre of a galaxy has a higher metallicity than the outskirts (e.g. Zaritsky et al. 1994; Moustakas et al. 2010; Sánchez et al. 2014; Pilyugin et al. 2014, 2019; González Delgado et al. 2015; Ho et al. 2015; Zheng et al. 2017; Goddard et al. 2017; Bresolin 2019; Bresolin et al. 2022).

At the same time, spiral galaxies that show no clear evidence of an interaction present a common metallicity gradient, if normalized to an appropriate scale-length, such as the disc effective radius (R_e , e.g. Sánchez et al. 2014), the disc scale-length (R_d , e.g. Garnett et al. 1997) and the isophotal radius (R_{25} , e.g. Zaritsky et al. 1994; Pilyugin et al. 2014, 2019; Ho et al. 2015; Bresolin 2019), and the slope is independent of galaxy properties, such as stellar mass, absolute magnitude, morphology, or whether a bar is present or not.

The simple chemical evolution model has been widely used in studies of the chemical evolution and SFHs of nearby disc galaxies (e.g. Tinsley 1980; Chang et al. 1999, 2012; Boissier & Prantzos 2000; Chiappini et al. 2001; Mollá & Díaz 2005; Kubryk et al. 2015; Kang et al. 2017; Bresolin 2019), making great progress in our understanding the formation and evolution of disc galaxies. Meanwhile, the SFH is a vital aspect of the formation and evolution of any disc galaxies, since it dominates its resulting stellar disc structure (Frankel et al. 2019). Thus, in this work, the simple chemical evolution model is adopted to study the chemical evolution and SFHs of M33-mass bulgeless spiral galaxies.

The main aim of this paper is to investigate the disc formation scenarios and stellar mass growth histories of M33-mass bulgeless spiral galaxies, as well as to study whether or not the model predicted results of these four galaxies can explain the MZR and the observed metallicity gradients. The chemical evolution and SFHs of M33, NGC 300 and NGC 2403 have been studied in our previous work by using the simple chemical evolution model (Kang et al. 2012, 2016, 2017). Therefore, before making comparative studies of these four galaxies, we should construct a simple chemical evolution model to explore the chemical evolution and SFH of NGC 7793 first.

The outline of this paper is organized as follows. Section 2 describes the main ingredients of the chemical evolution model. The observed data including radial profiles and global properties of atomic hydrogen (HI) gas, SFR, sSFR and gas-phase metallicity constraints of NGC 7793 are presented in Sect. 3. In Sect. 4, we investigate the chemical evolution and SFH of NGC 7793 by using the simple chemical evolution model, and provide the disc formation scenarios and stellar mass growth histories of M33-mass spiral galaxies by comparing the evolution and SFH of NGC 7793 with those of M33, NGC 300 and NGC 2403. Conclusions are given in Sect. 5.

2. Model

Similar to our previous work (Chang et al. 1999; Kang et al. 2012, 2016, 2017), a star-forming galaxy disc is assumed to gradually build up due to continuous infall of metal-free gas ($X = 0.7571, Y_p = 0.2429, Z = 0$) from its halo, and it is composed of a set of independently evolved concentric rings, in the sense that no radial mass flows is allowed in the model. In fact, such flows can take place in real galaxies as a result of the presence of the bars (Sellwood & Wilkinson 1993), redistribution of angular momentum owing to viscosity (Ferguson & Clarke 2001) and radial stellar migration (Roškar et al. 2008). In particular, the age-metallicity relationship in the solar neighbourhood of our Galaxy (e.g. Edvardsson et al. 1993; Haywood 2008; Schönrich & Binney 2009; Minchev & Famaey 2010; Feuillet et al. 2019; Xiang & Rix 2022) and the observed U-shaped colour profiles in galaxies (Azzollini et al. 2008; Bakos et al. 2008) put strong constraints on the presence of radial migration (e.g. Schönrich & Binney 2009; Minchev et al. 2012; Kubryk et al. 2013; Spitoni et al. 2015; Frankel et al. 2018; Buck 2020; Vincenzo & Kobayashi 2020; Chen et al. 2023). Moreover, the metal-enriched gas outflows are considered in the model, since both observations (Garnett 2002; Tremonti et al. 2004) and theoretical models (Erb 2008; Finlator & Davé 2008; Spitoni et al. 2020) showed that the gas outflow process plays a key role during the chemical evolution of low-mass galaxies with stellar mass $\log(M_*/M_\odot) < 10.5$. Finally, the model does not include the bulge nor does it differentiate between the thin and thick disc (see e.g. Grisoni et al. 2017; Spitoni et al. 2019). Despite the simplifying assumption of independently evolving rings, the model has been successfully applied to investigate the formation and evolution of the Milky Way disc and other nearby disc galaxies (Chang et al. 1999; Boissier & Prantzos 2000; Muñoz-Mateos et al. 2011; Kang et al. 2012, 2016, 2017; Bouquin et al. 2018; Bresolin 2019).

Thus, main ingredients of the model are including infalls of metal-free gas, star formation, metal production via stellar evolution, stellar mass return and outflows of metal-enriched gas. The details of these ingredients are presented in the following. The instantaneous recycling approximation (IRA, Tinsley 1980) is adopted in the model by assuming that the gas return from stars to the interstellar medium (ISM) happens on a short timescale compared with galactic evolution, and the gas is well mixed with stellar ejecta. Although IRA is a strong assumption in chemical evolution modelling, it still represents a good approximation for the abundance of chemical elements produced by massive stars with short lifetimes. The best example of such a chemical element is given by oxygen, which also represents the best proxy for the global metallicity of the galaxy ISM, since it is the most abundant heavy element by mass. On the other hand, the ISM evolution of chemical elements produced by stars with long lifetimes cannot be followed by chemical evolution models working with the IRA assumption. Examples of such chemical elements are given by nitrogen, carbon and iron. To consider the stellar lifetimes with a high level of detail, numerical chemical evolution models, in which the IRA is relaxed, should be adopted (see Matteucci 2012; Vincenzo et al. 2016).

The evolution in each ring can be described by the following differential equations from Tinsley (1980):

$$\frac{d[\Sigma_{\text{tot}}(r, t)]}{dt} = f_{\text{in}}(r, t) - f_{\text{out}}(r, t), \quad (1)$$

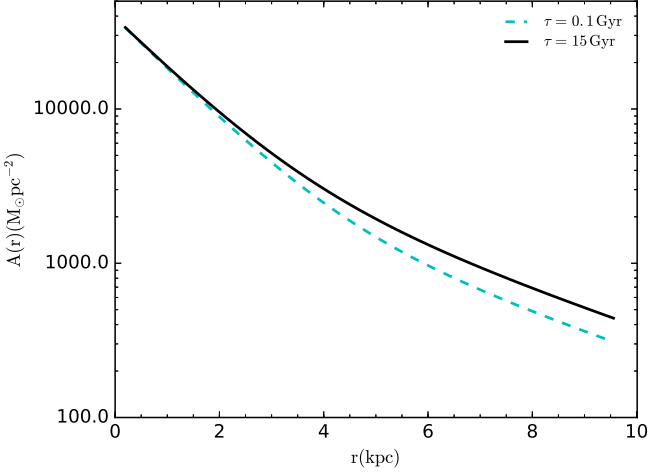


Fig. 1. $A(r)$ function. The dashed and solid lines are corresponding to two limiting cases of $\tau = 0.1$ Gyr and $\tau = 15$ Gyr, respectively. Note that, for the convenience of comparison, the $A(r)$ values of the model adopting $\tau = 15$ Gyr have been multiplied by 4000.

$$\frac{d[\Sigma_{\text{gas}}(r, t)]}{dt} = -(1 - R)\Psi(r, t) + f_{\text{in}}(r, t) - f_{\text{out}}(r, t), \quad (2)$$

$$\frac{d[Z(r, t)\Sigma_{\text{gas}}(r, t)]}{dt} = y(1 - R)\Psi(r, t) - Z(r, t)(1 - R)\Psi(r, t) + Z_{\text{in}}f_{\text{in}}(r, t) - Z_{\text{out}}(r, t)f_{\text{out}}(r, t), \quad (3)$$

where $\Sigma_{\text{tot}}(r, t)$ and $\Sigma_{\text{gas}}(r, t)$ are the total (star + gas) and gas mass surface density in the ring centered at galactocentric distance r at evolution time t , respectively; $\Psi(r, t)$ and $Z(r, t)$ are the SFR and metallicity in the corresponding place and time, respectively. $f_{\text{in}}(r, t)$ and $f_{\text{out}}(r, t)$ are the gas infall rate and the gas outflow rate in the corresponding place and time, respectively. R is the return fraction and y is the nuclear synthesis yield. Both R and y are functions of the initial mass function (IMF) and weakly depend on metallicity and time (Vincenzo et al. 2016). Neither metallicity nor time dependence of R and y will be further considered in our model, since the oxygen yield is independent of metallicity and the stellar lifetimes under our assumptions. Furthermore, galactic chemical enrichment depends significantly on the IMF (Vincenzo et al. 2016; Goswami et al. 2021) and the Kroupa et al. (1993) IMF is favoured in describing the chemical evolution of spiral discs (Romano et al. 2010; Vincenzo et al. 2016), therefore the IMF of Kroupa et al. (1993) is adopted in this work. The values of $R = 0.289$ and $y = 0.019$ are obtained by averaging the values of R and y_Z over metallicity in Table 2 of Vincenzo et al. (2016), corresponding to the compilation of stellar yields of Romano et al. (2010). Z_{in} is the metallicity of the infalling gas and assumed to be metal-free, i.e. $Z_{\text{in}} = 0$. $Z_{\text{out}}(r, t)$ is the metallicity of the outflowing gas and assumed to have the same metallicity as the ISM, i.e. $Z_{\text{out}}(r, t) = Z(r, t)$ (Chang et al. 2010; Belfiore et al. 2016; Kang et al. 2012, 2016, 2017, 2021).

The metal-free gas infall rate at each radius r and time t , $f_{\text{in}}(r, t)$, in units of $M_{\odot} \text{pc}^{-2} \text{Gyr}^{-1}$, as a function of space and time, is adopted as in Kang et al. (2012, 2016, 2017):

$$f_{\text{in}}(r, t) = A(r) \cdot t \cdot e^{-t/\tau}, \quad (4)$$

where τ is the gas infall timescale, and it is a free parameter in our model. The range of the free parameter τ is from 0.1 Gyr to 15.0 Gyr. As shown in Fig. 1 of Kang et al. (2016), the gas

infall rate we adopted in this work is low in the beginning and gradually increases with time. This gas infall rate reaches the maximal value when $t = \tau$ and then falls. The case of $\tau = 0.1$ Gyr is corresponding to a time-declining gas infall rate that most of the cold gas has been accreted to the disc in the early period of its history, while that of $\tau = 15.0$ Gyr represents a time-increasing gas infall rate that a large fraction of cold gas is now falling onto the disc of NGC7793. How we obtain the best-fitting value of τ will be presented in Sect. 4.1.

The function $A(r)$ is determined iteratively so that the present-day model predicted stellar mass surface density $\Sigma_{*}(r, t_{\text{g}})$ matches the observations (Kang et al. 2012, 2016, 2017). $\Sigma_{*}(r, t_{\text{g}})$ is well described by an exponential profile:

$$\Sigma_{*}(r, t_{\text{g}}) = \Sigma_{*}(0, t_{\text{g}})\exp(-r/R_{\text{d}}), \quad (5)$$

where R_{d} is the present-day disc scale-length. $\Sigma_{*}(0, t_{\text{g}})$ is the present-day central stellar mass surface density, and it can be easily obtained from $\Sigma_{*}(0, t_{\text{g}}) = M_{*}/2\pi R_{\text{d}}^2$. In this work, we adopt the stellar mass and disc scale-length of NGC 7793 as $M_{*} = 3.162 \times 10^9 M_{\odot}$ and $R_{\text{d}} = 1.3$ kpc, which are estimated from Infrared Array Camera (IRAC) images at $3.6 \mu\text{m}$ (Leroy et al. 2008). t_{g} is the cosmic age and we set $t_{\text{g}} = 13.5$ Gyr according to the standard flat cosmology.

In our calculation we adopt a value of the free parameter τ and then start with a first estimate of $A(r)$ and numerically solve Eqs. (1) and (2) adopting a SFR surface density $\Psi(r, t)$ (see below). By comparing the model predicted $\Sigma_{*}(r, t_{\text{g}})$ with its observed value, we adjust the value of $A(r)$ and repeat the calculation until the resulting $\Sigma_{*}(r, t_{\text{g}})$ fits the observed radial distribution. Figure 1 plots the model predicted radial profile of $A(r)$, where the dashed and solid lines are corresponding to two limiting cases of $\tau = 0.1$ Gyr and $\tau = 15$ Gyr, respectively. It should be emphasized that, for the convenience of comparison, the $A(r)$ values of the model adopting $\tau = 15$ Gyr have been multiplied by 4000. As can be seen from Fig. 1, $A(r)$ varies strongly with τ .

The SFR surface density $\Psi(r, t)$ (in units of $M_{\odot} \text{pc}^{-2} \text{Gyr}^{-1}$) describes how a disc galaxy of a given cold gas mass and scale radius will form its stars. Leroy et al. (2008) and Bigiel et al. (2008) have found that $\Psi(r, t)$ appears to correlate strongly with the molecular hydrogen gas mass surface density ($\Sigma_{\text{H}_2}(r, t)$) on sub-kpc scales, rather than the mass surface density of atomic hydrogen gas ($\Sigma_{\text{HI}}(r, t)$) or the total gas ($\Sigma_{\text{tot}}(r, t) = \Sigma_{\text{H}_2}(r, t) + \Sigma_{\text{HI}}(r, t)$). They also found that in their sample of spiral galaxies (including NGC 7793) the molecular hydrogen gas (H_2) forms stars at a roughly constant efficiency at radii where it can be detected (Leroy et al. 2008; Bigiel et al. 2008). $\Psi(r, t)$ proportional to $\Sigma_{\text{H}_2}(r, t)$ has been used in disc models by Lagos et al. (2011), Kang et al. (2012, 2016, 2017) and Kubryk et al. (2015), and it will be also adopted in this paper:

$$\Psi(r, t) = \Sigma_{\text{H}_2}(r, t)/t_{\text{dep}}, \quad (6)$$

Where t_{dep} is the molecular gas depletion time, and its value is adopted as $t_{\text{dep}} = 1.9$ Gyr in this work (Leroy et al. 2008; Bigiel et al. 2008). In order to split $\Sigma_{\text{gas}}(r, t)$ into $\Sigma_{\text{H}_2}(r, t)$ and $\Sigma_{\text{HI}}(r, t)$ in our galaxy evolution model, we adopt the semi-empirical prescription by Blitz & Rosolowsky (2006) and Leroy et al. (2008) for the molecular-to-atomic ratio:

$$R_{\text{mol}}(r, t) = \Sigma_{\text{H}_2}(r, t)/\Sigma_{\text{HI}}(r, t) = [P_{\text{h}}(r, t)/P_0]^{\alpha_{\text{P}}}, \quad (7)$$

where $P_{\text{h}}(r, t)$ is the mid-plane pressure of the ISM. P_0 and α_{P} are constants derived from the observations. We adopt $P_0/k = 1.7 \times 10^4 \text{cm}^{-3} \text{K}$ and $\alpha_{\text{P}} = 0.8$ (Leroy et al. 2008).

The mid-plane pressure of the ISM in disc galaxies can be expressed as (Elmegreen 1989; Leroy et al. 2008):

$$P_h(r, t) = \frac{\pi}{2} G \Sigma_{\text{gas}}(r, t) \left[\Sigma_{\text{gas}}(r, t) + \frac{c_{\text{gas}}}{c_*} \Sigma_*(r, t) \right], \quad (8)$$

where G is the gravitational constant, and c_{gas} and c_* are the (vertical) velocity dispersions of gas and stars, respectively. Observations reveal that c_{gas} is a constant along the disc and we adopt $c_{\text{gas}} = 11 \text{ km s}^{-1}$ (Ostriker et al. 2010), while c_* is estimated as $c_* = \sqrt{\frac{2\pi G R_d}{7.3} \Sigma_*(r, t)^{0.5}}$, see Appendix B.3 of Leroy et al. (2008) for more details.

The feedback from supernova gives rise to galactic outflows when the thermal energy of a galaxy exceeds the binding energy of gas. NGC 7793 is a low-mass disc galaxy with shallower gravitational potential, making it more susceptible to losing its ISM (Garnett 2002; Tremonti et al. 2004; Hirschmann et al. 2016; Lian et al. 2018a; Spitoni et al. 2021b). Thus, the gas-outflow process is important during the evolution and SFH of NGC 7793. We assume that the outflowing gas does not fall again to the disc, and its metallicity is equal to that of ISM at the time the outflow process is launched (Chang et al. 2010; Kang et al. 2012, 2016, 2017; Ho et al. 2015). The gas outflow rate $f_{\text{out}}(r, t)$ is proportional to $\Psi(r, t)$ (see Recchi et al. 2008; Spitoni et al. 2015, 2020):

$$f_{\text{out}}(r, t) = b_{\text{out}} \Psi(r, t). \quad (9)$$

where b_{out} is the gas outflow efficiency, and it is the other free parameter in our model. The assumption $f_{\text{out}}(r, t)$ proportional to $\Psi(r, t)$ is reasonable if supernova and winds of massive stars are the main drivers of the galactic wind.

In summary, the gas infall timescale τ and the gas outflow efficiency b_{out} are two free parameters in our model. The best-fitting model predicted τ and b_{out} obtained in Sect. 4.1 will be presented in Table 3. Moreover, a degeneracy between the yield y and the outflow parameter b_{out} exists in that the model adopting a higher y needs a larger b_{out} to reproduce the observed radial metallicity distribution. Thanks to the fact that the reasonable range of y is small for a fixed IMF (Vincenzo et al. 2016) compared with the large possible range of b_{out} , we can constrain b_{out} by using the observed metallicity gradient. It should be emphasized that, although the accurate value of free parameters in our best-fitting model may change a little, our results of the main trends of the SFHs of NGC 7793 are robust.

3. Observations

A successful chemical evolution model of NGC 7793, especially one involving free parameters, should reproduce as many observed constraints as possible, including both local (concerning the radial profiles) and global (concerning the whole disc) constraints. In that sense, the observed present-day cold gas, SFR, sSFR and metallicity distributions provide crucial constraints on the model. Thus, we summarise the current available observations for the disc of NGC 7793 in this section.

3.1. Radial distributions of gas mass, SFR, sSFR and metallicity

The stratification of atomic hydrogen (HI) of NGC 7793 is obtained from the Very Large Array (VLA) maps of the National Radio Astronomy Observatory (NRAO) (Walter et al. 2008), and the radial distribution HI mass surface density (Σ_{HI}) of

NGC 7793 is taken from Leroy et al. (2008). The radial SFR surface density (Σ_{SFR}) along the disc of NGC 7793 is estimated by the combination of FUV with $24 \mu\text{m}$ maps (Leroy et al. 2008) and by the FUV emission corrected by the WISE $22 \mu\text{m}$ (Casasola et al. 2017).

sSFR, defined as SFR per unit of stellar mass, represents the ratio of young to old stars and shows what fraction of total star formation has been occurred recently. Muñoz-Mateos et al. (2007) derived the radial sSFR profiles for NGC 7793 from GALEX and 2MASS (FUV– K) colour profiles after a proper SFR calibration of the UV luminosity and K -band mass-to-light ratio are adopted. Smith et al. (2021) calculated the radial sSFR profiles for NGC 7793 by using broad-band indicators for SFR (FUV + $24 \mu\text{m}$ flux) and stellar mass ($3.6 \mu\text{m}$ flux).

The present-day distribution of metallicity within an individual galaxy is the outcome of a complex pattern of evolution, advancing through infall of metal-free gas, star formation, energy feedback from stars and metal-enriched outflows. Each of these processes, to various extents, reshuffles the metals present in and around galaxy discs. Thus, the radial metallicity distribution of galaxies places important constraints on the galaxy chemical model (Boissier & Prantzos 2000; Ho et al. 2015; Kubryk et al. 2015; Kang et al. 2012, 2016, 2017, 2021; Bresolin 2019, and references therein). The radial metallicity gradient has been studied for a long time, starting with the pioneering work by Aller (1942). Most spiral galaxies in the local Universe exhibit negative metallicity gradients within their optical radius, i.e. the centre of a galaxy has a higher metallicity than the outskirts (e.g. Zaritsky et al. 1994; Rupke et al. 2010; Moustakas et al. 2010; Sánchez et al. 2014; Pilyugin et al. 2014; Kudritzki et al. 2015; Ho et al. 2015; Bresolin 2019).

Since oxygen is the most abundant metal by mass in the Universe, it is a good tracer for the total metal content. Oxygen is also an element for which the IRA approximation is appropriate, therefore oxygen abundance (i.e. $12 + \log(\text{O}/\text{H})$) will be used to represent the metallicity of NGC 7793 and adopt the solar value as $12 + \log(\text{O}/\text{H})_{\odot} = 8.69$ (Asplund et al. 2009) throughout this work. The absolute gas-phase metallicity depends on the calibrations used, and the classical T_e method is generally considered to provide the most reliable oxygen abundances in HII-regions (Izotov et al. 2006; Pilyugin et al. 2014). Thus, we use the oxygen abundances in HII-regions determined by the T_e method to constrain the model. The radial distribution of metallicity from HII-regions emission line analysis along the disc of NGC 7793 have been observed and quantified by many works (McCall et al. 1985; Zaritsky et al. 1994; Moustakas et al. 2010; Bibby & Crowther 2010; Pilyugin et al. 2014; Stanghellini et al. 2015), and the data from Bibby & Crowther (2010), Pilyugin et al. (2014) and Stanghellini et al. (2015) are used to constrain the model adopted in this work. The linear radial metallicity gradient depends on the galaxy distance, so we have scaled the metallicity gradient to the distance of 3.9 Mpc. The metallicity gradient of NGC 7793 is $-0.07 \pm 0.019 \text{ dex kpc}^{-1}$ and $-0.36 \pm 0.10 \text{ dex } R_{25}^{-1}$ (Bibby & Crowther 2010), $-0.0662 \pm 0.0104 \text{ dex kpc}^{-1}$ and $-0.350 \pm 0.055 \text{ dex } R_{25}^{-1}$ (Pilyugin et al. 2014), $-0.054 \pm 0.019 \text{ dex kpc}^{-1}$ and $-0.286 \pm 0.102 \text{ dex } R_{25}^{-1}$ (Stanghellini et al. 2015).

All the aforementioned observed radial distributions of HI mass, SFR, sSFR and metallicity will be displayed in Fig. 2 to constrain the model for searching for the best-fitting model of NGC 7793.

Table 1. Basic properties of NGC 7793, NGC 2403, NGC 300 and M33.

Property	NGC 7793	NGC 2403	NGC 300	M33
Morphology	SA(s)d ^{a,b}	SAB(s)cd ^{a,b}	SA(s)d ^{a,b}	SA(s)cd ^{a,b}
Distance (Mpc)	3.9 ^c	3.2 ^{d,e}	2.0 ^d	0.8 ^f
M_B (mag)	-18.7 ^g	-18.6 ^h	-17.66 ⁱ	-18.4 ⁱ
M_K (mag)	-19.40 ^j	-21.3 ^j	-20.1 ^j	-20.4 ^j
Scale-length (kpc)	1.3 ^k	1.6 ^k	1.29 ^l	1.4 ^l
Rotation velocity (km s ⁻¹)	116 ^m	136 ^m	91 ^m	110 ^m
Stellar mass (10 ⁹ M _⊙)	3.16 ^k	5.01 ^k	1.93 ^l	4.5 ^l

Refs: (a) NED; (b) de Vaucouleurs et al. (1991); (c) Karachentsev et al. (2004); (d) Dalcanton et al. (2009); (e) Freedman et al. (2001); (f) Williams et al. (2009); (g) Prugniel & Heraudeau (1998); (h) Lee et al. (2011); (i) Gogarten et al. (2010); (j) Jarrett et al. (2003); (k) Leroy et al. (2008); (l) Muñoz-Mateos et al. (2007); (m) Garnett (2002).

Table 2. Global observational data for the disc of NGC 7793.

Property	Value	References
HI mass	$\sim (1.05 - 1.26) \times 10^9 M_{\odot}$	1, 2
H ₂ mass	$\sim 2.0 \times 10^8 M_{\odot}$	2
Gas fraction	$\sim 0.27 - 0.33$	
Total SFR	$\sim 0.235 - 0.52 M_{\odot} \text{ yr}^{-1}$	1, 3, 4, 5, 6
sSFR	$\sim (8.06 - 9.74) \times 10^{-11} \text{ yr}^{-1}$	2, 7
$12 + \log(\text{O}/\text{H})_{R_e}$	$\sim 8.31 - 8.87$	3, 8, 9, 10

Refs: (1) Leroy et al. (2008); (2) Muraoka et al. (2016); (3) Bibby & Crowther (2010); (4) Kennicutt et al. (2011); (5) Skibba et al. (2011); (6) Calzetti et al. (2015); (7) Muñoz-Mateos et al. (2007); (8) Moustakas et al. (2010); (9) Pilyugin et al. (2014); (10) Stanghellini et al. (2015).

3.2. Global properties of gas mass, SFR, sSFR and metallicity

The atomic hydrogen (HI) gas mass of NGC 7793 is $M_{\text{HI}} = 1.26 \times 10^9 M_{\odot}$ (Leroy et al. 2008) and $M_{\text{HI}} = 1.05 \times 10^9 M_{\odot}$ (Muraoka et al. 2016). The molecular hydrogen (H₂) gas mass of NGC 7793 is $M_{\text{H}_2} = 2.0 \times 10^8 M_{\odot}$ (Muraoka et al. 2016). As a result, the gas fraction (f_{gas}) of NGC 7793 can be easily calculated through $f_{\text{gas}} = \frac{M_{\text{HI}} + M_{\text{H}_2}}{M_{\text{HI}} + M_{\text{H}_2} + M_{\star}}$, and the value of f_{gas} is $\sim 0.27 - 0.33$.

The current global SFR of NGC 7793 disc has been measured by using different tracers, $0.235 M_{\odot} \text{ yr}^{-1}$ from a combination of FUV with $24 \mu\text{m}$ maps by Leroy et al. (2008), $0.45 M_{\odot} \text{ yr}^{-1}$ from the observed $\text{H}\alpha + [\text{NII}]\lambda 6583$ flux by Bibby & Crowther (2010), $0.26 M_{\odot} \text{ yr}^{-1}$ from a combination of $\text{H}\alpha$ with $24 \mu\text{m}$ maps by Kennicutt et al. (2011), $0.363 M_{\odot} \text{ yr}^{-1}$ from a combination of FUV with total infrared (TIR) maps by Skibba et al. (2011), $0.52 M_{\odot} \text{ yr}^{-1}$ calculated from the GALEX FUV corrected for dust attenuation (Calzetti et al. 2015), and $0.251 M_{\odot} \text{ yr}^{-1}$ obtained from hybrids of FUV and $22 \mu\text{m}$ maps by Leroy et al. (2019).

The value of sSFR for NGC 7793 is $\sim (8.36 - 9.74) \times 10^{-11} \text{ yr}^{-1}$ derived by using FUV- K colour (Muñoz-Mateos et al. 2007) and $8.06 \times 10^{-11} \text{ yr}^{-1}$ estimated by Muraoka et al. (2016).

The value of metallicity at the effective radius of the disc $12 + \log(\text{O}/\text{H})_{R_e}$ is used as a surrogate for the mean metallicity of a galaxy (Zaritsky et al. 1994; Sánchez et al. 2013). R_e is equal to 1.685 times the radial scale-length R_d of the disc

(de Vaucouleurs & Pence 1978) and is basically corresponding to $0.4R_{25}$ (Sánchez et al. 2013) in the local Universe, i.e. $R_e = 1.685R_d = 0.4R_{25}$. The value of mean metallicity for the disc of NGC 7793 is 8.466 ± 0.05 (Bibby & Crowther 2010), 8.31 ± 0.02 (calibration of Kobulnicky & Kewley 2004) and 8.87 ± 0.01 (calibration of Pilyugin & Thuan 2005) (Moustakas et al. 2010), 8.378 ± 0.02 (Pilyugin et al. 2014) and 8.445 ± 0.063 (Stanghellini et al. 2015), respectively.

The above-mentioned global observed properties for the disc of NGC 7793 are summarised in Table 2.

4. Results and discussion

In this section, we firstly investigate the influence of the free parameters on model predictions and search for the best-fitting model for NGC 7793. Secondly, we study the properties of stellar populations along the disc of NGC 7793. Finally, to search for clues to the processes that drive the disc formation scenarios and stellar mass growth histories, we compare the best-fitting model predicted growth history of NGC 7793 with those of M33, NGC 300 and NGC 2403, which have been separately studied in our previous work (Kang et al. 2012, 2016, 2017).

4.1. Radial distributions

The aforementioned free parameters in the model are the gas infall timescale τ and the outflow efficiency b_{out} . We explore the influence of these two free parameters on the model predictions through comparing the model predictions with observations. The dotted, dashed and dot-dashed lines in Fig. 2 separately denote the predictions of the model adopting $(\tau, b_{\text{out}}) = (0.1 \text{ Gyr}, 0)$, $(\tau, b_{\text{out}}) = (15 \text{ Gyr}, 0)$ and $(\tau, b_{\text{out}}) = (15 \text{ Gyr}, 1.0)$. The left-hand side of Fig. 2 shows the radial profiles of HI mass (top) and SFR (bottom) surface density, and the right-hand side of Fig. 2 displays the radial profiles of sSFR (top) and metallicity (bottom). The details of the observed data were presented in Sect. 3.

The comparison of the three models in Fig. 2 shows that the outflow efficiency has a strong influence on metallicity but only a small effect on HI column density, SFR and sSFR, while the gas infall timescale is important for the radial distribution of all four quantities. This is mainly due to the fact that, during the whole evolutionary history of a galaxy, the infalling gas supplies the reservoir for star formation, while the outflowing gas takes a fraction of metals away from the disc. Figure 2 also shows that the area between the dotted line $(\tau, b_{\text{out}}) = (0.1 \text{ Gyr}, 0)$ and the dot-dashed line $(\tau, b_{\text{out}}) = (15 \text{ Gyr}, 1.0)$ brackets almost the

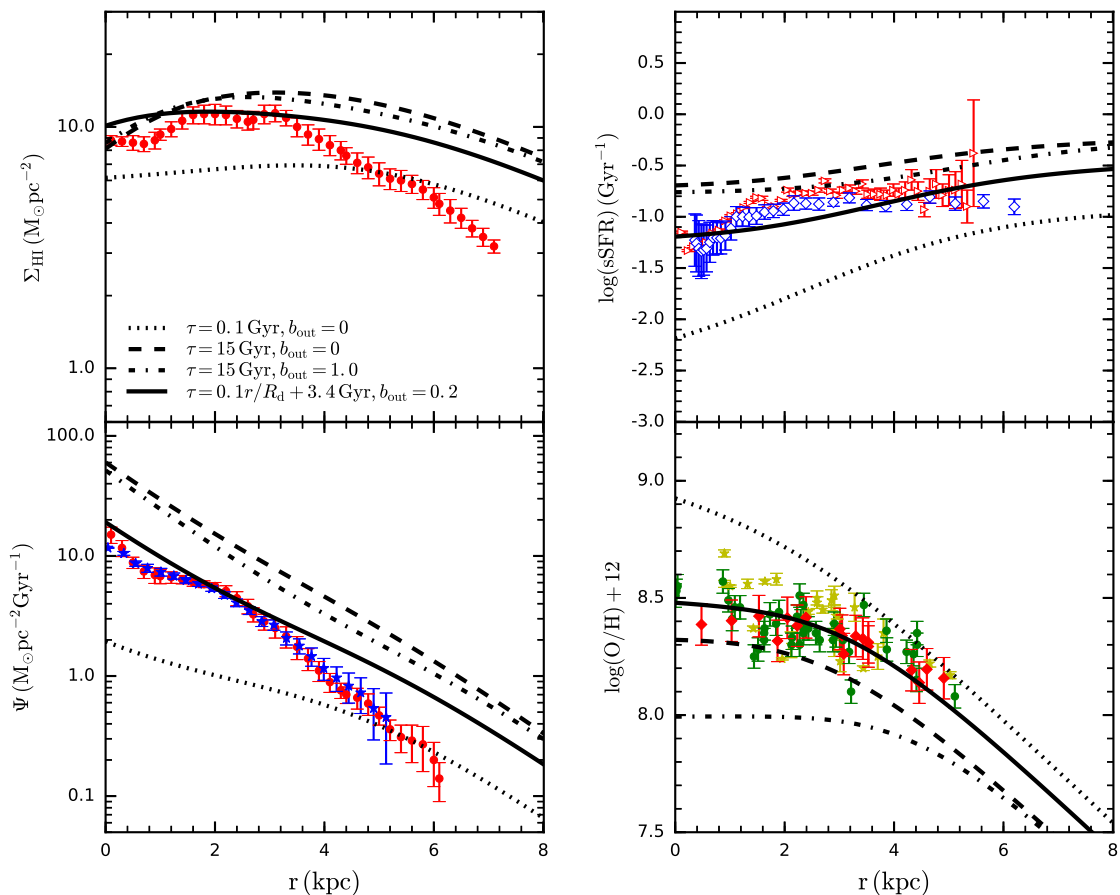


Fig. 2. Comparisons of the model predictions with the observations. Different line types correspond to different parameter groups: dotted lines $(\tau, b_{\text{out}}) = (0.1 \text{ Gyr}, 0)$, dashed lines $(\tau, b_{\text{out}}) = (15 \text{ Gyr}, 0)$, dot-dashed lines $(\tau, b_{\text{out}}) = (15 \text{ Gyr}, 1.0)$, solid lines $(\tau, b_{\text{out}}) = (0.1r/R_d + 3.4 \text{ Gyr}, 0.2)$. On the left-hand side, the radial profiles of H I mass and SFR surface density are shown in the top and bottom panels, respectively; On the right-hand side, the radial profiles of sSFR and metallicity are displayed in the top and bottom panels, respectively. Different symbols are corresponding to the observed data taken from different works. H I data from Leroy et al. (2008) are shown by red filled circles. SFR data from Leroy et al. (2008) are denoted as red filled circles, while those from Casasola et al. (2017) are displayed by blue filled asterisks. sSFR data from Muñoz-Mateos et al. (2007) and Smith et al. (2021) are denoted as red open triangles and red open diamonds, respectively. $12 + \log(\text{O}/\text{H})$ data taken from Bibby & Crowther (2010), Pilyugin et al. (2014) and Stanghellini et al. (2015) are separately plotted by yellow filled asterisks, green filled circles and red filled diamonds.

whole region of the observed data, which implies that it is possible to construct a model that can reproduce the main observed features of NGC 7793 disc.

The right bottom panel of Fig. 2 exhibits negative metallicity gradient, i.e. the central region has a higher metallicity than the outskirts, consistent with the disc inside-out formation scenario. Moreover, the colour–magnitude diagrams (CMD)-derived SFH also certifies an inside-out growth for the disc of NGC 7793 (Sacchi et al. 2019). Thus, following the method adopted in our previous work (Kang et al. 2012, 2016, 2017), the form of infall timescale is assumed to be $\tau(r) = a \times r/R_d + b$, namely that gas takes longer timescale to settle onto the disc in the outer regions, where a and b are the coefficients for $\tau(r)$. An inside-out growth mechanism originally introduced in the theory of galaxy evolution on the basis of chemical evolution models (Larson 1976; Matteucci & Francois 1989) and semianalytic model of disc galaxies in the context of dark matter cosmologies (Kauffmann 1996; van den Bosch 1998). Adding the aforementioned free parameter b_{out} , there are now three free parameters (a , b and b_{out}) in our model that should be determined.

In order to search for the best combination of free parameters (a , b and b_{out}) able to reproduce the main observed fea-

tures of NGC 2403, we use the classical χ^2 technique by comparing the model results with the corresponding observational data, such as the radial profiles of H I gas mass surface density, SFR, sSFR and $12 + \log(\text{O}/\text{H})$. The boundary conditions of a , b and b_{out} for NGC 7793 are separately assumed to be $0 < a \leq 3.0$, $1.0 \leq b \leq 5.0$ and $0.1 \leq b_{\text{out}} \leq 0.9$. In practise, for each pair of a and b , we vary the value of b_{out} to calculate the minimum value of χ^2 , which corresponds to the best combination of a , b and b_{out} , and we obtain $(a, b, b_{\text{out}}) = (0.1, 3.4, 0.2)$, i.e. $(\tau, b_{\text{out}}) = (0.1r/R_d + 3.4 \text{ Gyr}, 0.2)$ defined as the best-fitting model, and the best combination of free parameters are displayed in Table 3. The best-fitting model predicted results are plotted by solid lines in Fig. 2. It can be found that there is remarkable agreement between the model results and the NGC 7793 observations.

The right lower panel of Fig. 2 shows that the best-fitting model predicted radial metallicity distribution does not show a constant gradient of $12 + \log(\text{O}/\text{H})$. Instead there is a bend in the radial metallicity distribution. This is mainly due to the fact that we use the observational data, such as the radial distributions of gas mass surface density, SFR surface density, sSFR and $12 + \log(\text{O}/\text{H})$, to constrain the model and to search for the best-

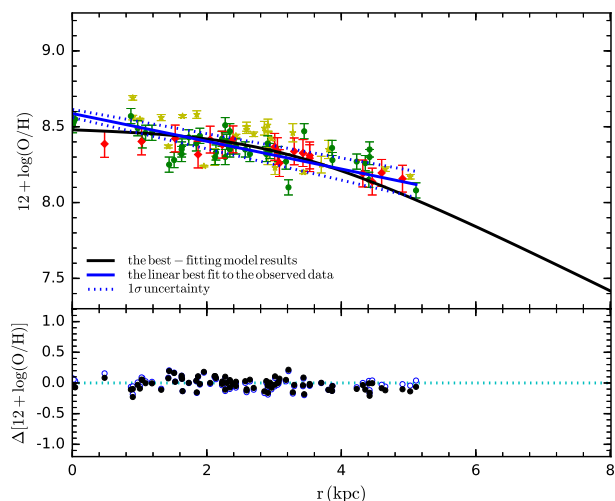


Fig. 3. Radial distribution of $12 + \log(\text{O}/\text{H})$. Upper panel: comparisons of the present-day radial distribution of $12 + \log(\text{O}/\text{H})$ predicted by our best-fitting model (black solid line) with the observational data. Different symbols denote the observed metallicity data from different works: yellow filled asterisks (Bibby & Crowther 2010), green filled circles (Pilyugin et al. 2014) and red filled diamonds (Stanghellini et al. 2015). The linear best fit to the observed data and 1σ uncertainty are plotted as the blue solid and dotted lines, respectively. Lower panel: the black filled circles show the deviations of the observations from our best-fitting model predictions, derived by the black solid line minus the observed data in the above panel, while the blue open circles show the ones obtained from the linear best fit minus the observational data in the above panel.

fitting model which can simultaneously reproduce these observational data for NGC 7793. In order to further state the best-fitting model can nicely describe the formation and evolution of NGC 7793, comparisons of the best-fitting model predicted present-day $12 + \log(\text{O}/\text{H})$ distributions (black solid line) with the observed data (points) are displayed in the upper panel of Fig. 3. The linear best fit and the 1σ uncertainty of the observed data are also shown in this panel by the blue solid line and blue dotted lines, respectively. The deviations of the observed $12 + \log(\text{O}/\text{H})$ points from our best-fitting model predicted $12 + \log(\text{O}/\text{H})$, calculated by the best-fitting model predictions minus the observed data, are shown as the black filled circles in the lower panel of Fig. 3, and the deviations of the observed metallicity data from the corresponding linear best fit are also plotted in this panel as the blue open circles. It can be found from the lower panel of Fig. 3 that there is little difference between the black solid circles and the blue open circles. The mean deviation values of the black filled circles and the blue open circles are 0.019 and 0.015, respectively. Figure 3 reinforces our results that the best-fitting model includes and describes reasonably the crucial ingredients of the main physical processes that regulate the formation and evolution history of NGC 7793.

4.2. Stellar populations along the disc

To investigate the stellar populations along the disc of NGC 7793, Figure 4 demonstrates the best-fitting model predicted SFHs (upper panel) and stellar mass growth curves (lower panel) of three regions at different galactocentric distances for NGC 7793. Different line types represent different regions along the disc, red dotted line for 1–2 kpc, blue dashed line for 4–5 kpc

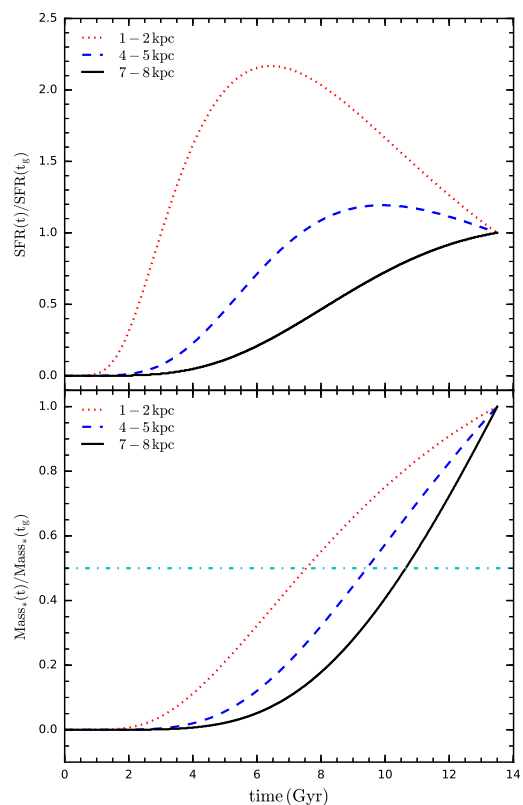


Fig. 4. Star formation histories (upper panel) and relative stellar mass growth (lower panel) of three regions at different galactocentric distances (1–2 kpc, 4–5 kpc, 7–8 kpc) for NGC 7793 disc. Both the SFRs and stellar masses are normalized by their present-day values. The horizontal dash-dotted line in the lower panel remarks when each component achieves 50% of its final value.

and black solid line for 7–8 kpc. The horizontal cyan dash-dotted line in the lower panel marks when each component reaches 50% of its final value. Both the SFRs and stellar masses in Fig. 4 are normalized by their present-day values. The upper panel of Fig. 4 shows that the peak of the SFH moves to later time from internal to more external regions of the disc, and regions at larger radii have more extended SFHs. The lower panel demonstrates that the stellar mass growth rate in the inner region is faster than that in the outer region. Figure 4 shows clear signatures of inside-out growth for NGC 7793 disc.

If the disc of NGC 7793 does form "inside-out", one would expect to see negative radial gradient in age. Figure 5 shows the mean stellar age along the disc of NGC 7793 predicted by the best-fitting model with solid line. It can be found that the stellar population in the inner region of the disc is older than that in the outer region, that is, the inner parts of the disc have a higher percent of old stars than in the outer parts. The mean stellar age which decreases with radius is indeed consistent with the inside-out growth scenario for the disc formation. In this picture, the inner regions of NGC 7793 are built up at earlier times than outer parts, and as a result contain on average older stars than outermost regions. The results presented in both Fig. 4 and Fig. 5 are indicative of an inside-out formation scenario for the disc of NGC 7793, in line with the observed results derived by Muñoz-Mateos et al. (2007) and Sacchi et al. (2019).

The solid line in Fig. 6 displays the best-fitting model predicted growth history of stellar mass for NGC 7793, and stellar

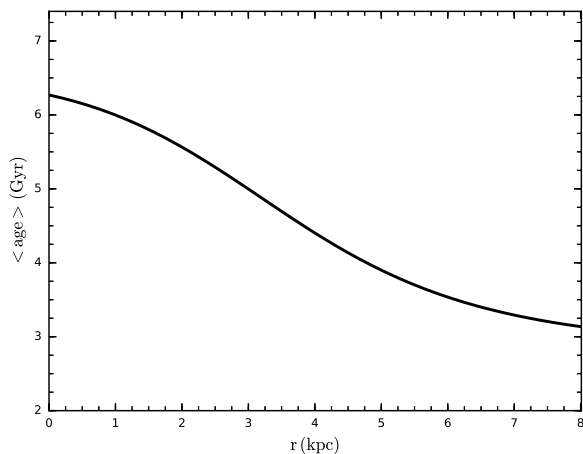


Fig. 5. Radial profile of mean stellar age along the disc of NGC 7793 predicted by its own best-fitting model.

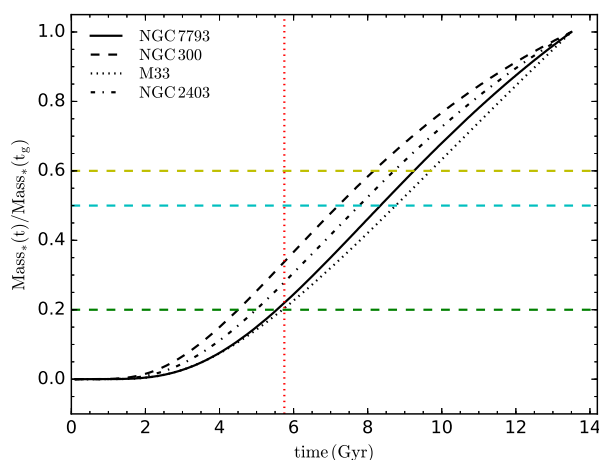


Fig. 6. Stellar mass growth histories of NGC 7793 (solid line), NGC 300 (dashed line), M33 (dotted line) and NGC 2403 (dash-dotted line) predicted by their own best-fitting models. Stellar masses are normalized to their present-day values. The horizontal dashed lines mark when the stellar mass reaches 20%(green), 50%(cyan) and 60%(yellow) of its final value, while the vertical red dotted line denotes the galaxy evolutionary age at $t = 5.75$ Gyr (i.e. $z = 1$).

mass is normalized to its present-day value. To make the stellar mass growth rate more visible, the horizontal dashed lines separately mark when the stellar mass reaches 20% (green), 50% (cyan) and 60%(yellow) of its final value. The vertical red dotted line denotes the galaxy evolutionary age at $t = 5.75$ Gyr (i.e. $z = 1$). It can be found that the resulting stellar mass growth history displays a relatively smooth build-up of its stellar mass. The best-fitting model results also show that about 80% of the stellar mass of NGC 7793 is assembled within the last 8 Gyr and 40% within the last 4 Gyr, consistent with what found by the CMD-derived SFH for NGC 7793 in Radburn-Smith et al. (2012) and Sacchi et al. (2019). Other line types in this Figure will be discussed in the Sect. 4.3.1.

4.3. Comparison with other three disc galaxies

NGC 7793, M33, NGC 300 and NGC 2403 are four bulgeless disc galaxies with similar morphology and stellar mass, and the chemical evolution and SFHs of NGC 300, M33 and NGC 2403

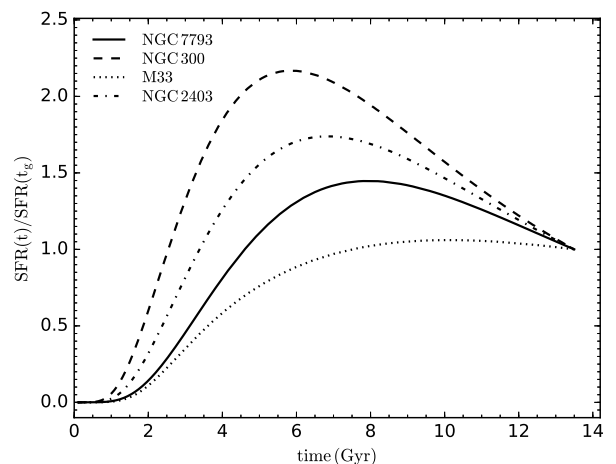


Fig. 7. Evolution of SFR for NGC 7793 (solid line), NGC 300 (dashed line), M33 (dotted line) and NGC 2403 (dash-dotted line) predicted by their own best-fitting models. SFRs are normalized to their present-day values.

have already been studied in our previous works (see Kang et al. 2012, 2016, 2017). In this section, we will compare the best-fitting model predicted SFH of NGC 7793 with those of M33, NGC 300 and NGC 2403 to search for clues to the processes that drive the disc formation scenarios and stellar mass growth histories. Table 3 summarises the input properties (including the total stellar mass M_* and the scale-length R_d), and the best-fitting parameters for the main ingredients of the models, such as the star formation law, the gas infall rate and outflow rate. Physical details of the model description and searching for the best-fitting models for M33, NGC 300 and NGC 2403 are separately in Kang et al. (2012, 2016, 2017).

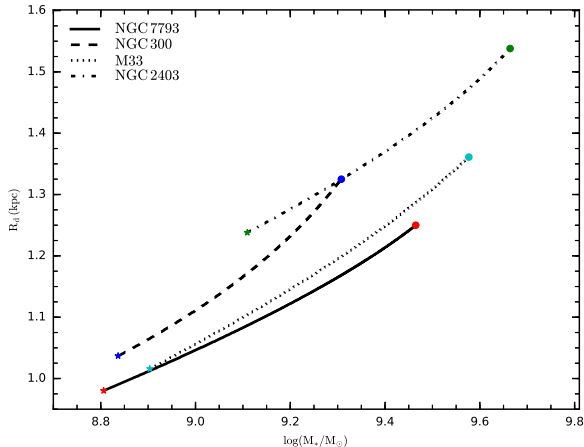
4.3.1. Evolution of stellar mass and SFR

Figure 6 plots the best-fitting model predicted growth history of stellar mass for NGC 7793 (solid line), NGC 300 (dashed line), M33 (dotted line) and NGC 2403 (dash-dotted line) and stellar masses is normalized to their present-day values. It can be found from Fig. 6 that they have also been steadily assembling their stellar mass. Our results are in qualitative agreement with the results in Fig 17 (bottom) of Sextl et al. (2023), who used the galaxy evolution model in Kudritzki et al. (2021) and found the galaxy stellar masses at 10 Gyr ago are significantly smaller than the final stellar masses. Figure 6 also shows that about 78 percent (NGC 7793), 66 percent (NGC 300), 72 percent (NGC 2403) and 79 percent (M33) galaxy's stars were formed between $z = 1$ and $z = 0$, that is, these four galaxies accumulated more than 50 percent of their total stellar mass within the past ~ 8 Gyr (i.e. $z = 1$), supported by the previous results that late-type galaxies with stellar mass $M_* < 10^{11} M_\odot$ appear to assembled most of their stellar mass at $z < 1$ (Leitner & Kravtsov 2011; Sachdeva et al. 2015), since stellar mass contributes to the majority of the total baryonic budget at most epochs ($z = 1$).

The best-fitting model predicted SFHs of these four galaxies are plotted in Fig. 7, and different line types are corresponding to different galaxies: solid line for NGC 7793, dashed line for NGC 300, dotted line for M33 and dash-dotted line for NGC 2403. Fig. 7 shows that the SFHs of NGC 7793, NGC 2403 and NGC 300 reach their peaks around 5.5 \sim 8 Gyr ago and then slowly drops down to its present-day value, while SFH of M33 reaches a maximum about 4 Gyr ago and then stays constant un-

Table 3. The main input properties and parameters of the best-fitting models for NGC 7793, NGC 2403, NGC 300 and M33.

Individual		NGC 7793	NGC 2403	NGC 300	M33	
Input physical properties		M_* ($10^9 M_\odot$)	3.16	5.0	1.928	4.0
		R_d (kpc)	1.3	1.6	1.29	1.4
Star formation law	$\Psi(r, t) = \Sigma_{H_2}(r, t)/t_{\text{dep}}$	t_{dep} (Gyr)	1.9	1.9	1.9	0.46
Infall rate	$f_{\text{in}}(r, t) \propto t \cdot e^{-t/\tau}$	$\tau(r)$ (Gyr)	$0.1r/R_d + 3.4$	$0.2r/R_d + 3.2$	$0.35r/R_d + 2.47$	$r/R_d + 5.0$
Outflow rate	$f_{\text{out}}(r, t) = b_{\text{out}}\Psi(r, t)$	b_{out}	0.2	0.6	0.9	0.5


Fig. 8. Evolution of the scale-length and total stellar mass predicted by our best-fitting models for NGC 7793 (solid line), NGC 300 (dashed line), M33 (dotted line) and NGC 2403 (dash-dotted line). Each track follows the evolution of a galaxy from $z = 1$ (the $z = 1$ step is marked with asterisk) to $z = 0$ (the $z = 0$ step is marked with filled circle).

til recently before declining somewhat. The more extended SFHs of M33 further indicates that the principal time of star formation on the discs of NGC 7793, NGC 2403 and NGC 300 is earlier than that on the disc of M33. This may be due to an HI bridge between M33 and M31, in accordance with the statistical result of Guglielmo et al. (2015) that galaxies of a given mass have different SFHs depending on their environment.

4.3.2. Evolution of scale-length R_d

Figure 8 plots the evolution of the scale-length and total stellar mass (mass-size relation) from $z = 1$ to $z = 0$ for NGC 7793 (solid line), NGC 300 (dashed line) and M33 (dotted line), NGC 2403 (dot-dashed line). The $z = 0$ step and $z = 1$ step is marked with filled circle and asterisk, respectively. As in Muñoz-Mateos et al. (2011), the disc scale-length R_d at evolution time t is computed by fitting an exponential law to the total stellar mass surface density profile, $\Sigma_*(r, t) = \Sigma_*(0, t)\exp(-r/R_d(t))$. The model predicts $R_d = 1.25$ kpc for NGC 7793, which is in agreement with its observed value $R_d = 1.30$ kpc (Leroy et al. 2008), considering the observed uncertainties. It can be seen from Fig. 8 that stellar mass and scale-length simultaneously increase as time goes by, that is, these four spirals grow in size while they grow in mass, in perfect agreement with the previous mass-size trend (e.g. Muñoz-Mateos et al. 2011; Pezzulli et al. 2015; Sachdeva & Saha 2016). However, the details about how stellar discs form and grow in mass and size are not known from first principles and significant observa-

tional effort is still required to shed light on the missing links from structure formation to galaxy formation.

Investigating the rate at which stellar discs grow does shed light on the interplay between the physical processes, such as metal-free gas infall, star formation, enriched gas outflows, and the global evolution of disc galaxies (Frankel et al. 2019). The specific stellar mass growth rate (ν_M) and specific radial scale-length growth rate (ν_R) represent the stellar mass and radial scale-length growth rates, defined as $dM_*/dt = \frac{M_*(z=0) - M_*(z=1)}{t(z=0) - t(z=1)}$ and $dR_d/dt = \frac{R_d(z=0) - R_d(z=1)}{t(z=0) - t(z=1)}$, normalized to the actual present-day value of stellar mass $M_*(z = 0)$ and scale-length $R_d(z = 0)$. Therefore, ν_R between $z = 1$, (i.e. $t = 5.75$ Gyr) and $z = 0$ (i.e. $t = 13.5$ Gyr) calculated by their own best-fitting models are separately 0.0278 Gyr^{-1} for NGC 7793, 0.0281 Gyr^{-1} for NGC 300, 0.0252 Gyr^{-1} for NGC 2403 and 0.0327 Gyr^{-1} for M33. We notice that all these four disc galaxies have undergone a radial scale-length growth of $\sim 20\% - 25\%$ since $z = 1$ until now, in perfect agreement with what found by Muñoz-Mateos et al. (2011) and Pezzulli et al. (2015). At the same time, ν_M from $z = 1$ to $z = 0$ are 0.1007 Gyr^{-1} for NGC 7793, 0.0854 Gyr^{-1} for NGC 300, 0.0931 Gyr^{-1} for NGC 2403 and 0.1016 Gyr^{-1} for M33. Comparing ν_R and ν_M , we conclude that these four disc galaxies grow in size at ~ 0.30 times the rate at which they grow in mass, not far from the value ~ 0.32 derived by Courteau et al. (2007) and ~ 0.35 found by Pezzulli et al. (2015). Furthermore, the values of both ν_M and ν_R for M33 are larger than that for other three galaxies, indicating that recently there are more star formation occurred along the M33 disc than that in other three galaxies. This is mainly due to the fact that HI bridge between M33 and M31 may be responsible for supplying cold gas for star formation in the disc of M33 (Wolfe et al. 2013).

4.3.3. Stellar mass-Metallicity relation

The shape of MZR provides important constraints for understanding the chemical evolution of galaxies. Figure 9 shows a comparison of MZR predicted by our best-fitting models with results measured by other authors. In order to compare our best-fitting model predicted MZR with that of young stellar population and individual supergiant stars, we first scale the mean metallicities of these galaxies to solar ratios, i.e. $[Z] = 12 + \log(\text{O}/\text{H})_{\text{gal}} - (12 + \log(\text{O}/\text{H})_\odot) = 12 + \log(\text{O}/\text{H})_{\text{gal}} - 8.69$. Thus, the best-fitting model predicted mean metallicities (defined as the metallicity at the effective radius R_e) are separately -0.336 (NGC 7793), -0.161 (NGC 2403), -0.234 (NGC 300) and -0.208 (M33), and their values are shown in Fig. 9 and denoted as black star (NGC 7793), red triangle (NGC 2403), blue square (NGC 300) and magenta diamond (M33). In Fig. 9 we plot the MZR based on abundance data obtained from the analysis of quantitative spectroscopy of individual objects in 17 nearby galaxies (see Fig. 9 and Table 4 in Bresolin et al. 2022):

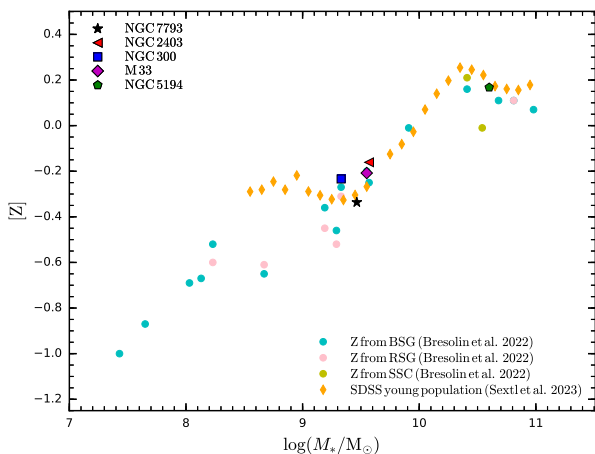


Fig. 9. Comparison of the stellar mass-metallicity relation predicted by our best-fitting models (black star for NGC 7793, red triangle for NGC 2403, blue square for NGC 300, magenta diamond for M33 and green pentagon for NGC 5194) with that published in the literature. Solid circles are stellar metallicity of nearby galaxies measured from spectroscopy of individual blue supergiants (cyan), red supergiants (pink) and super star clusters (yellow) (see Bresolin et al. 2022, reference therein). The orange thin-diamonds are the MZR derived from young stellar population of SDSS star-forming galaxies (Sextl et al. 2023).

blue supergiant stars (BSG, cyan circles), red supergiant stars (RSG, pink circles) and super star clusters (SSC, yellow circles). In this Figure, we also display the MZR derived by Sextl et al. (2023, orange thin-diamonds) from the young stellar population of SDSS local star-forming galaxies. For comparison, the mean metallicity of NGC 5194 (Kang et al. 2015, green pentagon) is also plotted in Fig. 9.

It can be seen from Fig. 9 that our model predicted MZR of these galaxies (including NGC 5194) are in accordance with the MZR derived by both young stellar population of SDSS star-forming galaxies and individual young massive supergiant stars (including super star clusters) data. Although our best-fitting models are constrained by the metallicities from HII-regions emission line analysis, the model predicted MZR is compatible with the empirical MZR measured from individual supergiant stars in nearby galaxies and young stellar population in SDSS star-forming galaxies.

4.3.4. Metallicity gradient-Stellar mass

The dependence of metallicity gradient on galaxy stellar mass is a matter of recent controversy. Isolated spiral galaxies share a characteristic metallicity gradient when normalized to an appropriate scale-length, such as R_d , R_e or R_{25} (Zaritsky et al. 1994; Garnett et al. 1997; Sánchez et al. 2014; Bresolin & Kennicutt 2015; Ho et al. 2015; Lian et al. 2018b; Pilyugin et al. 2019; Bresolin 2019). On the other hand, Belfiore et al. (2017, based on MaNGA) and Poetrodjojo et al. (2018, based on SAMI) find that the metallicity gradient in terms of $\text{dex } R_e^{-1}$ steepens with galaxy stellar mass until $\log(M_*/M_\odot) \sim 10.5$ and remains roughly constant for higher masses. In addition, the metallicity gradients in interacting disc galaxies are shallower than that in isolated disc galaxies due to effective mixing (e.g. Kewley et al. 2010; Rupke et al. 2010; Torrey et al. 2012).

Indeed, Pilyugin et al. (2014) measured the metallicity of 130 nearby late-type galaxies and derived a common metallicity

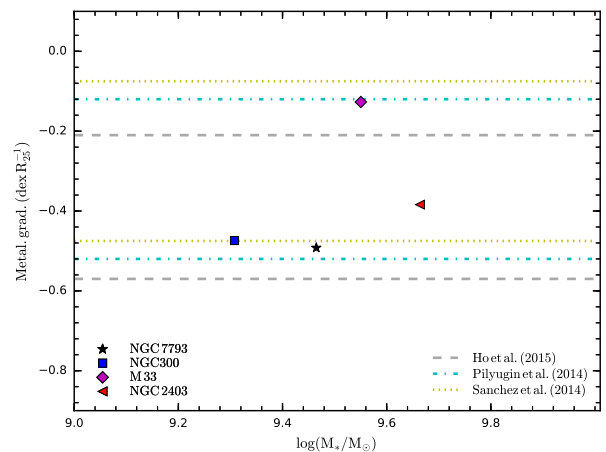


Fig. 10. Metallicity gradient versus stellar mass predicted by their own best-fitting models when the metallicity gradients are measured in $\text{dex } R_{25}^{-1}$: NGC 7793 (black star), NGC 2403 (red triangle), NGC 300 (blue square) and M33 (magenta diamond). Different line types represent observed metallicity gradients from different authors: dashed lines (Ho et al. 2015), dotted lines (Sánchez et al. 2014), and dash-dotted lines (Pilyugin et al. 2014).

gradient of $0.32 \pm 0.20 \text{ dex } R_{25}^{-1}$ for 104 of their field galaxies (i.e. excluding mergers and close pairs). Sánchez et al. (2014) found that 146 galaxies from CALIFA that show no clear evidence of an interaction present a common metallicity gradient expressed in terms of $\text{dex } R_e^{-1}$ with a value $-0.11 \pm 0.08 \text{ dex } R_e^{-1}$, independent of morphology, the existence of a bar, absolute magnitude or mass. Ho et al. (2015) also studied 49 local field isolated spiral galaxies with absolute magnitudes $-22 < M_B < -16$, and found evidence for a common metallicity gradient among their galaxies when the slope is expressed in units of the isophotal radius R_{25} , i.e. $-0.39 \pm 0.18 \text{ dex } R_{25}^{-1}$. Pilyugin et al. (2019) analysed 147 galaxies from MaNGA and found the metallicity gradient independent of galaxy stellar with the mean value $-0.2 \text{ dex } R_{25}^{-1}$. Bresolin (2019) derived the common metallicity gradient with a value $-0.34 \pm 0.2 \text{ dex } R_{25}^{-1}$ based on long-slit observations of nearby spiral galaxies. To compare the best-fitting model predicted observed metallicity gradient with the observed common metallicity gradient, one must consider the different scale-lengths. According to the relation between R_e and R_{25} , i.e. $R_e = 0.4R_{25}$ (Zaritsky et al. 1994; Sánchez et al. 2013), we can convert the common metallicity gradient in Sánchez et al. (2014, 146 isolated spiral galaxies from CALIFA) to $-0.275 \pm 0.2 \text{ dex } R_{25}^{-1}$.

All the aforementioned information indicates it is worthwhile to investigate the metallicity gradients for the discs of NGC 7793, NGC 300, M33 and NGC 2403. Both Fig. 3 of NGC 7793 in this work and Fig. 2 of NGC 2403 in Kang et al. (2017) show that the linear best fit to the observed data within the optical radius almost coincides with our best-fitting model predicted metallicity distributions. Here, we also calculate the metallicity gradients of these four galaxies within their optical radii, and the corresponding values predicted by their own best-fitting models are separately $-0.492 \text{ dex } R_{25}^{-1}$ for NGC 7793, $-0.384 \text{ dex } R_{25}^{-1}$ for NGC 2403, $-0.474 \text{ dex } R_{25}^{-1}$ for NGC 300 and $-0.127 \text{ dex } R_{25}^{-1}$ for M33. The metallicity gradient of NGC 7793 agrees well with its observations (Bibby & Crowther 2010; Pilyugin et al. 2014; Stanghellini et al. 2015). Interestingly, although the models for NGC 300 in Kang et al. (2016) and NGC 2403 in Kang et al. (2017) were constrained by

observed metallicities from HII-region emission line analysis (Bresolin et al. 2009, NGC 300) and (Berg et al. 2013, NGC 2403), their best-fitting model predicted results are in excellent agreement with the observed metallicity distributions and gradients from stellar spectral analysis of young massive supergiant stars (Kudritzki et al. 2008; Gazak et al. 2015, NGC 300) and (Bresolin et al. 2022, NGC 2403). For M33, some new observational metallicity data obtained from HII-region emission line analysis (e.g. Alexeeva & Zhao 2022; Rogers et al. 2022) and stellar spectral analysis of young massive blue supergiant stars (Liu et al. 2022) were recently appeared, it would be interesting to consider these metallicities to constrain the chemical evolution model of M33. Fortunately, our best-fitting model results of M33 (Kang et al. 2012) is basically in agreement with these observations, taking into account the observed uncertainties and the calibration for determining metallicity. It should be emphasized that, although the accurate values of free parameters in our best-fitting models are not unique, the main results may not impact our conclusion significantly.

Figure 10 displays metallicity gradient versus stellar mass. The best-fitting model predictions are shown as black star (NGC 7793), red triangle (NGC 2403), blue square (NGC 300) and magenta diamond (M33). Different line types in this Figure represent observed metallicity gradients (expressed in $\text{dex } R_{25}^{-1}$) from different authors: dashed lines (Ho et al. 2015), dotted lines (Sánchez et al. 2014) and dash-dotted lines (Pilyugin et al. 2014). It can be seen that the best-fitting model predicted metallicity gradients exactly reproduce the observed data. The metallicity gradients of isolated spiral galaxies NGC 7793, NGC 2403 and NGC 300 are similar and steeper than that of M33, the later is the same behaviour found by Rupke et al. (2010), that is, the metallicity gradient in isolated galaxies is steeper than that in interacting galaxies, since the interactions between M33 and M31 may change its metallicity gradient. The similar metallicity gradients in NGC 7793, NGC 2403 and NGC 300 indicate that they may follow very similar chemical evolution when growing their discs (Prantzos & Boissier 2000; Ho et al. 2015).

5. Conclusions

NGC 7793 is an isolated loosely bound member of the Sculptor Group, with no bar and a very faint central bulge. In this work, we build a bridge for the disc of NGC 7793 between its observed properties and its evolutionary history by constructing a simple chemical evolution model. Our results show that the model predictions are very sensitive to the adopted infall timescale, but the outflow process mainly influences the metallicity distributions along the disc of NGC 7793, since it takes a fraction of metals away from NGC 7793 disc due to its shallower gravitational potential. The best-fitting model results show that the disc of NGC 7793 forms inside-out, in excellent agreement with the general predictions of the inside-out growth scenario for the evolution of spiral galaxies. About 80% of the stellar mass of NGC 7793 is assembled within the last 8 Gyr and 40% within the last 4 Gyr.

We also compared the best-fitting model results of NGC 7793 with those of M33, NGC 300 and NGC 2403, which are studied in our previous work (Kang et al. 2012, 2016, 2017). We found that 78% (NGC 7793), 72% (NGC 300), 66% (NGC 2403) and 79% (M33) galaxy's stars were formed between $z = 1$ and $z = 0$, that is, these four galaxies accumulated more than 50 percent of their total stellar mass within the past ~ 8 Gyr (i.e. $z = 1$). Our results also show that these four disc galaxies simultaneously increase their sizes and stellar masses

as time goes by, and they grow in size at ~ 0.30 times the rate at which they grow in mass, providing a perfect match to the previous results (Courteau et al. 2007; Pezzulli et al. 2015). The best-fitting model predicted MZR and gradients, constrained by the observed metallicities from HII-region emission line analysis, are in excellent agreement with the metallicities measured from individual massive red and blue supergiant stars.

Acknowledgements. We thank the anonymous referee for constructive comments and suggestions, which improved the quality of our work greatly. Xiaoyu Kang and Fenghui Zhang are supported by the National Key R&D Program of China with (Nos. 2021YFA1600403 and 2021YFA1600400), the National Natural Science Foundation (NSF) of China (No. 11973081, 11573062, 11403092, 11773063), the Basic Science Centre project of the NSF of China (No. 12288102), the Science Research grants from the China Manned Space Project (No. CMS-CSST-2021-A08), International Centre of Supernovae, Yunnan Key Laboratory (No. 202302AN360001), the NSF of Yunnan Province (No. 2019FB006). Rolf Kudritzki acknowledges support by the Munich Excellence Cluster Origins Funded by the Deutsche Forschungsgemeinschaft (DFG, German Research Foundation) under the German Excellence Strategy EXC-2094 390783311.

References

- Aller, L. H. 1942, *ApJ*, 95, 52
 Alexeeva, S. & Zhao, G. 2022, *ApJ*, 925, 76
 Andrews, B. H. & Martini, P. 2013, *ApJ*, 765, 140
 Asplund, M., Grevesse, N., Sauval, A. J., & Scott, P. 2009, *ARA&A*, 47, 481
 Aumer, M. & Binney, J. J. 2009, *MNRAS*, 397, 1286
 Azzollini, R., Trujillo, I., & Beckman, J. E. 2008, *ApJ*, 679, L69
 Bakos, J., Trujillo, I., & Pohlen, M. 2008, *ApJ*, 683, L103
 Baldry, I. K., Glazebrook, K., & Driver, S. P. 2008, *MNRAS*, 388, 945
 Baldry, I. K., Driver, S. P., Loveday, J., et al. 2012, *MNRAS*, 421, 621
 Barnes, J. E. & Hernquist, L. 1992, *ARA&A*, 30, 705
 Bauer, A. E., Hopkins, A. M., Gunawardhana, M., et al. 2013, *MNRAS*, 434, 209
 Behroozi, P., Wechsler, R. H., Hearin, A. P., et al. 2019, *MNRAS*, 488, 3143
 Belfiore, F., Maiolino, R., & Bothwell, M. 2016, *MNRAS*, 455, 1218
 Belfiore, F., Maiolino, R., Tremonti, C., et al. 2017, *MNRAS*, 469, 151
 Berg, D. A., Skillman, E. D., Garnett, D. R., et al. 2013, *ApJ*, 775, 128
 Bibby, J. L. & Crowther, P. A. 2010, *MNRAS*, 405, 2737
 Bigiel, F., Leroy, A., Walter, F., et al. 2008, *AJ*, 136, 2846
 Blitz, L. & Rosolowsky, E. 2006, *ApJ*, 650, 933
 Boissier, S. & Prantzos, N. 2000, *MNRAS*, 312, 398
 Bouquin, A. Y. K., Gil de Paz, A., Muñoz-Mateos, J. C., et al. 2018, *ApJS*, 234, 18
 Bresolin, F., Gieren, W., Kudritzki, R.-P., et al. 2009, *ApJ*, 700, 309
 Bresolin, F. & Kennicutt, R. C. 2015, *MNRAS*, 454, 3664
 Bresolin, F. 2019, *MNRAS*, 488, 3826
 Bresolin, F., Kudritzki, R.-P., & Urbaneja, M. A. 2022, *ApJ*, 940, 32
 Brinchmann, J., Charlot, S., White, S. D. M., et al. 2004, *MNRAS*, 351, 1151
 Buck, T. 2020, *MNRAS*, 491, 5435
 Byun, Y. I. & Freeman, K. C. 1995, *ApJ*, 448, 563
 Calzetti, D., Lee, J. C., Sabbi, E., et al. 2015, *AJ*, 149, 51
 Casasola, V., Cassarà, L. P., Bianchi, S., et al. 2017, *A&A*, 605, A18
 Chang, R. X., Hou, J. L., Shu, C. G., & Fu, C. Q. 1999, *A&A*, 350, 38
 Chang, R. X., Hou, J. L., Shen, S. Y., & Shu, C. G. 2010, *ApJ*, 722, 380
 Chang, R. X., Shen, S. Y., & Hou, J. L. 2012, *ApJ*, 753, L10
 Chen, B., Hayden, M. R., Sharma, S., et al. 2023, *MNRAS*, 523, 3791
 Chiappini, C., Matteucci, F., & Romano, D. 2001, *ApJ*, 554, 1044
 Courteau, S., Dutton, A. A., van den Bosch, F. C., et al. 2007, *ApJ*, 671, 203
 Dalcanton, J. J., Williams, B. F., Seth, A. C., et al. 2009, *ApJS*, 183, 67
 de Vaucouleurs, G. & Pence, W. D. 1978, *AJ*, 83, 1163
 de Vaucouleurs, G., de Vaucouleurs, A., Corwin, H. G., et al. 1991, *S&T*, 82, 621
 Edvardsson, B., Andersen, J., Gustafsson, B., et al. 1993, *A&A*, 500, 391
 Elmegreen, B. G. 1989, *ApJ*, 338, 178
 Erb, D. K. 2008, *ApJ*, 674, 151
 Ferguson, A. M. N. & Clarke, C. J. 2001, *MNRAS*, 325, 781
 Feuillet, D. K., Frankel, N., Lind, K., et al. 2019, *MNRAS*, 489, 1742
 Finlator, K. & Davé, R. 2008, *MNRAS*, 385, 2181
 Frankel, N., Rix, H.-W., Ting, Y.-S., et al. 2018, *ApJ*, 865, 96
 Frankel, N., Sanders, J., Rix, H.-W., et al. 2019, *ApJ*, 884, 99
 Fraternali, F. & Tomassetti, M. 2012, *MNRAS*, 426, 2166
 Freedman, W. L., Madore, B. F., Gibson, B. K., et al. 2001, *ApJ*, 553, 47
 Gallazzi, A., Charlot, S., Brinchmann, J., et al. 2005, *MNRAS*, 362, 41
 Garnett, D. R., Shields, G. A., Skillman, E. D., et al. 1997, *ApJ*, 489, 63
 Garnett, D. R. 2002, *ApJ*, 581, 1019

- Gazak, J. Z., Kudritzki, R., Evans, C., et al. 2015, *ApJ*, 805, 182
- Goddard, D., Thomas, D., Maraston, C., et al. 2017, *MNRAS*, 466, 4731
- Gogarten, S. M., Dalcanton, J. J., Williams, B. F., et al. 2010, *ApJ*, 712, 858
- González Delgado, R. M., García-Benito, R., Pérez, E., et al. 2015, *A&A*, 581, A103
- Goswami, S., Slemer, A., Marigo, P., et al. 2021, *A&A*, 650, A203
- Grisoni, V., Spitoni, E., Matteucci, F., et al. 2017, *MNRAS*, 472, 3637
- Grisoni, V., Spitoni, E., & Matteucci, F. 2018, *MNRAS*, 481, 2570
- Guglielmo, V., Poggianti, B. M., Moretti, A., et al. 2015, *MNRAS*, 450, 2749
- Haywood, M. 2008, *MNRAS*, 388, 1175
- Hirschmann, M., De Lucia, G., & Fontanot, F. 2016, *MNRAS*, 461, 1760
- Ho, I.-T., Kudritzki, R.-P., Kewley, L. J., et al. 2015, *MNRAS*, 448, 2030
- Izotov, Y. I., Stasińska, G., Meynet, G., et al. 2006, *A&A*, 448, 955
- Jarrett, T. H., Chester, T., Cutri, R., et al. 2003, *AJ*, 125, 525
- Kang, X., Chang, R., Yin, J., et al. 2012, *MNRAS*, 426, 1455
- Kang, X., Chang, R., Zhang, F., et al. 2015, *MNRAS*, 449, 414
- Kang, X., Zhang, F., Chang, R., Wang, L., & Cheng, L. 2016, *A&A*, 585, A20
- Kang, X., Zhang, F., & Chang, R. 2017, *MNRAS*, 469, 1636
- Kang, X., Chang, R., Kudritzki, R.-P., et al. 2021, *MNRAS*, 502, 1967
- Karachentsev, I. D., Karachentseva, V. E., Huchtmeier, W. K., et al. 2004, *AJ*, 127, 2031
- Kauffmann, G. 1996, *MNRAS*, 281, 475
- Kelvin, L. S., Driver, S. P., Robotham, A. S. G., et al. 2014, *MNRAS*, 444, 1647
- Kennicutt, R. C., Calzetti, D., Aniano, G., et al. 2011, *PASP*, 123, 1347
- Kewley, L. J. & Ellison, S. L. 2008, *ApJ*, 681, 1183
- Kewley, L. J., Rupke, D., Zahid, H. J., et al. 2010, *ApJ*, 721, L48
- Kobulnicky, H. A. & Kewley, L. J. 2004, *ApJ*, 617, 240
- Kroupa, P., Tout, C. A., & Gilmore, G. 1993, *MNRAS*, 262, 545
- Kubryk, M., Prantzos, N., & Athanassoula, E. 2013, *MNRAS*, 436, 1479
- Kubryk, M., Prantzos, N., & Athanassoula, E. 2015, *A&A*, 580, A126
- Kudritzki, R.-P., Urbaneja, M. A., Bresolin, F., et al. 2008, *ApJ*, 681, 269
- Kudritzki, R.-P., Ho, I.-T., Schruha, A., et al. 2015, *MNRAS*, 450, 342
- Kudritzki, R.-P., Teklu, A. F., Schulze, F., et al. 2021, *ApJ*, 910, 87
- Lagos, C. D. P., Baugh, C. M., Lacey, C. G., et al. 2011, *MNRAS*, 418, 1649
- Larson, R. B. 1976, *MNRAS*, 176, 31
- Lee, J. C., Gil de Paz, A., Kennicutt, R. C., et al. 2011, *ApJS*, 192, 6
- Leitner, S. N. & Kravtsov, A. V. 2011, *ApJ*, 734, 48
- Leroy, A. K., Walter, F., Brinks, E., et al. 2008, *AJ*, 136, 2782
- Leroy, A. K., Sandstrom, K. M., Lang, D., et al. 2019, *ApJS*, 244, 24
- Lian, J., Thomas, D., & Maraston, C. 2018a, *MNRAS*, 481, 4000
- Lian, J., Thomas, D., Maraston, C., et al. 2018b, *MNRAS*, 476, 3883
- Liu, C., Kudritzki, R.-P., Zhao, G., et al. 2022, *ApJ*, 932, 29
- Matteucci, F. & Francois, P. 1989, *MNRAS*, 239, 885
- Matteucci, F. 2012, *Chemical Evolution of Galaxies: , Astronomy and Astrophysics Library. ISBN 978-3-642-22490-4. Springer-Verlag Berlin Heidelberg, 2012*
- McCall, M. L., Rybski, P. M., & Shields, G. A. 1985, *ApJS*, 57, 1
- Minchev, I. & Famaey, B. 2010, *ApJ*, 722, 112
- Minchev, I., Famaey, B., Quillen, A. C., et al. 2012, *A&A*, 548, A126
- Mollá, M. & Díaz, A. I. 2005, *MNRAS*, 358, 521
- Moustakas, J., Kennicutt, R. C., Tremonti, C. A., et al. 2010, *ApJS*, 190, 233
- Muñoz-Mateos, J. C., Gil de Paz, A., Boissier, S., et al. 2007, *ApJ*, 658, 1006
- Muñoz-Mateos, J. C., Boissier, S., Gil de Paz, A., et al. 2011, *ApJ*, 731, 10
- Muraoka, K., Takeda, M., Yanagitani, K., et al. 2016, *PASJ*, 68, 18
- Ostriker, E. C., McKee, C. F., & Leroy, A. K. 2010, *ApJ*, 721, 975.
- Pan, Z., Peng, Y., Zheng, X., et al. 2019, *ApJ*, 876, 21
- Panther, B., Jimenez, R., Heavens, A. F., et al. 2008, *MNRAS*, 391, 1117
- Pezzulli, G., Fraternali, F., Boissier, S., et al. 2015, *MNRAS*, 451, 2324
- Pilyugin, L. S. & Thuan, T. X. 2005, *ApJ*, 631, 231
- Pilyugin, L. S., Grebel, E. K., & Kniazev, A. Y. 2014, *AJ*, 147, 131
- Pilyugin, L. S., Grebel, E. K., Zinchenko, I. A., et al. 2019, *A&A*, 623, A122
- Poetrodojo, H., Groves, B., Kewley, L. J., et al. 2018, *MNRAS*, 479, 5235
- Prantzos, N. & Boissier, S. 2000, *MNRAS*, 313, 338
- Prugniel, P. & Heraudeau, P. 1998, *A&AS*, 128, 299
- Qu, Y., Helly, J. C., Bower, R. G., et al. 2017, *MNRAS*, 464, 1659
- Radburn-Smith, D. J., Roškar, R., Debattista, V. P., et al. 2012, *ApJ*, 753, 138
- Recchi, S., Spitoni, E., Matteucci, F., et al. 2008, *A&A*, 489, 555
- Rogers, N. S. J., Skillman, E. D., Pogge, R. W., et al. 2022, *ApJ*, 939, 44
- Romano, D., Karakas, A. I., Tosi, M., et al. 2010, *A&A*, 522, A32
- Roškar, R., Debattista, V. P., Stinson, G. S., et al. 2008, *ApJ*, 675, L65
- Rupke, D. S. N., Kewley, L. J., & Chien, L.-H. 2010, *ApJ*, 723, 1255
- Sacchi, E., Cignoni, M., Aloisi, A., et al. 2019, *ApJ*, 878, 1
- Sachdeva, S., Gadotti, D. A., Saha, K., et al. 2015, *MNRAS*, 451, 2
- Sachdeva, S. & Saha, K. 2016, *ApJ*, 820, L4
- Sánchez, S. F., Rosales-Ortega, F. F., Jungwiert, B., et al. 2013, *A&A*, 554, A58
- Sánchez, S. F., Rosales-Ortega, F. F., Iglesias-Páramo, J., et al. 2014, *A&A*, 563, A49
- Schönrich, R. & Binney, J. 2009, *MNRAS*, 396, 203
- Sellwood, J. A. & Wilkinson, A. 1993, *Reports on Progress in Physics*, 56, 173
- Sextl, E., Kudritzki, R.-P., Zahid, H. J., et al. 2023, *ApJ*, 949, 60
- Skibba, R. A., Engelbracht, C. W., Dale, D., et al. 2011, *ApJ*, 738, 89
- Smith, M. V., van Zee, L., Salim, S., et al. 2021, *MNRAS*, 505, 3998
- Spitoni, E., Romano, D., Matteucci, F., et al. 2015, *ApJ*, 802, 129
- Spitoni, E., Cescutti, G., Minchev, I., et al. 2019, *A&A*, 628, A38
- Spitoni, E., Calura, F., Mignoli, M., et al. 2020, *A&A*, 642, A113
- Spitoni, E., Verma, K., Silva Aguirre, V., et al. 2021a, *A&A*, 647, A73
- Spitoni, E., Calura, F., Silva Aguirre, V., et al. 2021b, *A&A*, 648, L5
- Stanghellini, L., Magrini, L., & Casasola, V. 2015, *ApJ*, 812, 39
- Thomas, D., Maraston, C., Schawinski, K., et al. 2010, *MNRAS*, 404, 1775
- Tinsley, B. M. 1980, *Fund. Cosmic Phys.*, 5, 287
- Torrey, P., Cox, T. J., Kewley, L., et al. 2012, *ApJ*, 746, 108
- Tremonti, C. A., Heckman, T. M., Kauffmann, G., et al. 2004, *ApJ*, 613, 898
- van den Bosch, F. C. 1998, *ApJ*, 507, 601
- Vincenzo, F., Matteucci, F., Belfiore, F., et al. 2016, *MNRAS*, 455, 4183
- Vincenzo, F. & Kobayashi, C. 2020, *MNRAS*, 496, 80
- Walter, F., Brinks, E., de Blok, W. J. G., et al. 2008, *AJ*, 136, 2563
- Williams, B. F., Dalcanton, J. J., Dolphin, A. E., et al. 2009, *ApJ*, 695, L15
- Williams, B. F., Dalcanton, J. J., Johnson, L. C., et al. 2011, *ApJ*, 734, L22
- Williams, B. F., Dalcanton, J. J., Stilp, A., et al. 2013, *ApJ*, 765, 120
- Wolfe, S. A., Pisano, D. J., Lockman, F. J., et al. 2013, *Nature*, 497, 224
- Xiang, M. & Rix, H.-W. 2022, *Nature*, 603, 599
- Zahid, H. J., Dima, G. I., Kudritzki, R.-P., et al. 2014, *ApJ*, 791, 130
- Zahid, H. J., Kudritzki, R.-P., Conroy, C., et al. 2017, *ApJ*, 847, 18
- Zaritsky, D., Kennicutt, R. C., & Huchra, J. P. 1994, *ApJ*, 420, 87
- Zheng, Z., Wang, H., Ge, J., et al. 2017, *MNRAS*, 465, 4572